Word Count: 8483

Carbon nanofiber dispersion in alkali solution and its reinforcement of alkali-activated volcanic ash-based geopolymers

Rongrong Zhang[1], Feng Li[1], Siqi Zhou[1*], Yue Hou[2]

[1]*School of Transportation Science and Engineering, Beihang University, Beihang University, Beijing, 100191, China*

[2]*Department of Civil engineering, Faculty of Science and Engineering, Swansea University, Swansea, SA2 8PP, UK*

[*] Corresponding author. E-mail:zsq47@buaa.edu.cn, Tel: +8618601266994

Abstract

Volcanic ash has several negative impacts on the environment and can be used in massive to synthesize geopolymers, which are considered quasi-brittle. Carbon nanofibers (CNFs) can reinforce the geopolymers, and the dispersion of CNFs directly determines the reinforcement effect. However, the dispersion of CNFs in alkali solutions is challenging. In this paper, the effect of surfactant type, dosage, and ultrasonic time on CNFs dispersion in aqueous and alkali solutions was investigated by the quantitive method of microscopic image processing to determine the preferred dispersion scheme. Zeta potential tests and visual observation were used to analyze the mechanism and stability. Based on this, volcanic ash-based geopolymer nanocomposites with 0.1 wt% contents of CNFs were synthesized. The mechanical properties were tested, and the microstructure was characterized using Scanning Electron Microscope coupled with Energy Dispersive Spectroscopy and Mercury Intrusion Porosimetry. The results showed that methylcellulose (MC), polycarboxylate superplasticizer (PC), and polyvinylpyrrolidone (PVP) could disperse CNFs in aqueous, but evident aggregations can be observed in the alkali solution. PC performed better than MC and PVP in alkali solutions, with 4.83% aggregation area of the whole image, 86% of 0-100 μm^2 aggregations, and an average aggregation area of 87 μm^2, beneficial from the comb-like structures. Dispersed CNFs can improve the 28-d flexural and compressive strength of the resulting geopolymer nanocomposite by 23% and 16%, respectively, and refine the pore structure through filling, bridging, and nucleation effects, decreasing the average pore size and porosity by 33% and 15%. This paper will contribute to the resourceful use of volcanic ash to reduce pollution and the higher reinforcement of CNFs in alkali-activated geopolymers.

Keywords: Volcanic ash, Geopolymer, Carbon nanofibers, Dispersion, Mechanical properties

1. Introduction

Volcanic ashes are fragments less than 2 mm in diameter formed by magma condensed during volcanic

30   eruptions (Rose and Durant, 2009). The reservation of volcanic ash is abundant due to volcanic activity

31   worldwide (Djobo et al., 2017). However, several environmental problems are caused by volcanic ash,

32   including water pollution, heavy metals, and air pollution (Horwell and Baxter, 2006; Wygel et al., 2019).

33   Therefore, the resourceful use of volcanic ash in massive is necessary. Geopolymers are an environmentally

34   friendly way to use volcanic ash with less energy consumption and lower carbon footprint compared to cement

35   production and are beneficial to reduce pollution, land occupation problems and global warming (Djobo and

36   Stephan, 2022; Wang, Y. et al., 2021; Zhang et al., 2021; Zhou et al., 2021).

37   It has been reported that cementitious materials, including geopolymers, have the disadvantages of low

38   tensile strength and poor strain capacity, often presenting brittle damage (Konsta-Gdoutos et al., 2010; Pan et

39   al., 2011), and the problem gets further aggravated due to the pozzolanic effect of precursors of

40   geopolymerization (Farhan et al., 2021). Adding fibers can inhibit the development of cracks and reinforce

41   cementitious materials (Bai et al., 2020; El-Sayed and Shaheen, 2020; Kan et al., 2020). Carbon nanofibers

42   (CNFs) are considered an excellent reinforcer. They can improve the mechanical properties and toughness at

43   the microscopic scale and are well reflected in flexural strength due to their small size, high strength, high

44   aspect ratio, and large specific surface area (Shi et al., 2019).

45   The uniform dispersion of CNFs is the key and prerequisite for acting as reinforcement and interacting

46   with the geopolymer (Aslani and Wang, 2019; Zhao et al., 2018). Several physical and chemical methods are

47   investigated to improve the dispersion in aqueous, including mechanical stirring, ball milling, ultrasonic

48   treatment, acid functionalization, and adding surfactants(Yazdanbakhsh et al., 2010; Yuan et al., 2017). The

49   most commonly used dispersion method combines adding surfactants and ultrasonication.

50   However, some researchers proposed that carbon nanomaterials (CNMs) may re-agglomerate in alkaline

51   environments, although they were well-dispersed in aqueous. The aggregations would not only affect the

52   reinforcement function of CNMs but also possibly lead to defects (Lu and Zhong, 2022). Recently, the research

53   mainly focused on graphene oxide (GO) and carbon nanotubes (CNTs) dispersing in cement pore solution but

54   limited to CNFs. Zhao et al. (2018) investigated the influence of different water reducing agents on GO

55   dispersion in cement pore solution. The results showed that polycarboxylate superplasticizer performs superior

56   to sodium lignosulfonate and b-naphthalene sulfonate formaldehyde in dispersing GO uniformly. Chuah et al.

57   (2018) suggested that the high alkalinity of the solution and high concentration of Ca^{2+} are the main factors

58   for the aggregation of GO in cement pore solution. And polycarboxylate, air entrainer, and Gum Arabic

59   promise to the dispersion. Jiang et al. (2003) prepared CNT aqueous solution and studied the variation of

60   CNTs dispersion with pH. It was found that the surfactant sodium dodecyl sulfate significantly fails to adsorb

61   on the CNTs resulting in agglomerations when pH is above 8. Stephens et al. (2016) proposed that although

62   re-aggregation of CNFs occurs regardless of the dispersion method, the dosage of the surfactant and CNFs,

63   the surfactant can beneficially affect the size and distribution of the aggregations.

64   For geopolymers, the commonly used alkali activators are sodium hydroxide (NaOH), potassium

65   hydroxide, sodium silicate, and other solutions at 6-14 mol/L concentrations, whose alkalinity is significantly

66   higher than cement pore solution. Also, the higher Na^+ concentration in alkali activators would be another

67   factor for the aggregation (Heister et al., 2010; Zhao et al., 2020). However, to the best of the authors'

68   knowledge, only one research is available on the dispersion of CNMs in alkali activator solutions.

69   Davoodabadi et al. (2021) compared the dispersions of CNTs in sodium silicate and NaOH solutions and

70   claimed that a smaller agglomeration size appears in the Na_2SiO_3 based nanofluid.

71   Therefore, considering the high concentration and strong alkalinity of the alkali activator solutions and

72   the changed agglomerations caused by the structural distinctions between CNFs, GO and, CNTs, it is vital to

73   compare the dispersion effects of different surfactants in alkali activators and preferably select a favorable

74   dispersion scheme for the promotion of CNF-reinforced volcanic ash-based geopolymers. In this paper, the

75   number, area, and particle size distribution of CNF aggregations in CNF-aqueous and CNF-NaOH solutions

76   were quantitatively characterized by microscopic image processing to determine the proper dispersion scheme,

77   including the surfactant type, dosage, and ultrasonic time. The dispersion mechanism was analyzed in

78   combination with the zeta potential test. Then, the volcanic ash-based geopolymer nanocomposites with 0 and

79   0.1% CNFs were prepared through the preferred scheme. The mechanical properties of the nanocomposites

80   were investigated, and microstructures were characterized by a Scanning Electron Microscope coupled with

81   Energy Dispersive Spectroscopy (SEM-EDS) and Mercury Intrusion Porosimetry (MIP) test to verify the

82   reinforcement effect of dispersed CNFs.

83   **2. Materials and methods**

84   **2.1 Materials**

85   The CNFs used in this study were XFM60, 50-200 nm in diameter and 1-15 μm in length, produced by

86   chemical vapor deposition (Nanjing XFNANO Technology, Nanjing, China). Their physical properties are

87   shown in Table 1.

Table 1 Properties of CNFs.

| Commercial name	Length (μm)	Diameter (nm)	Purity (%)	Tap density (g/cm³)	True density (g/cm³)	Specific surface area (m²/g)
XFM60	1-15	50-200	>95%	0.0431	2.1	>18

Since the geopolymerization reaction environment is strongly alkaline and ionic surfactants are more

susceptible to high ionic concentration(Sargam et al., 2021), three commonly used commercially available

nonionic surfactants, methylcellulose(MC), polycarboxylate superplasticizer (PC), and polyvinylpyrrolidone

(PVP) were selected. MC was purchased from Shanghai Aladdin Biochemical Technology (Shanghai, China)

with a viscosity factor of 15 mPa·s, Sika 540P PC with a comb-like molecular structure was from Shanghai

Chenqi Chemical Technology Co (Shanghai, China), and polyvinylpyrrolidone (PVP) with a relative

molecular weight of 8000 and a K value of 16-18 was from Shanghai Aladdin Biochemical Technology

(Shanghai, China). The appearance of the three surfactants is a white powder, and their molecular structures

are shown in Figure 1. Also, a control group was set up to disperse CNFs directly in aqueous and NaOH

solutions without surfactant.

(a) MC   (b) PC   (c) PVP
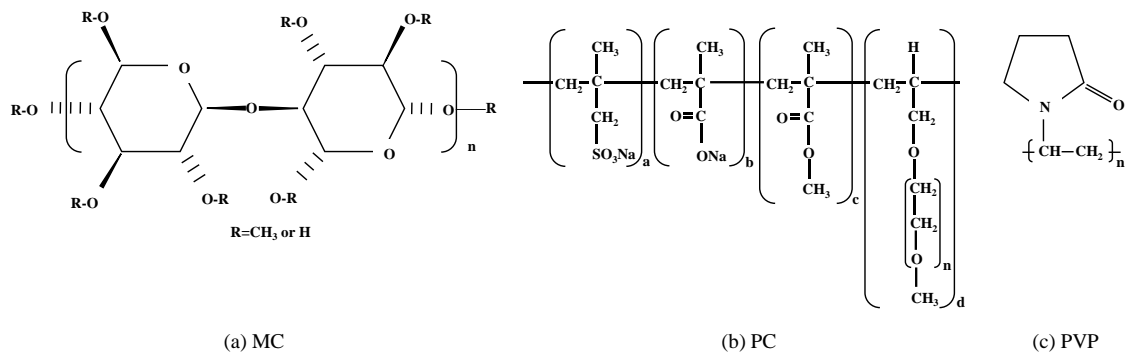
Figure 1 Molecular structure of (a) MC, (b) PC, and (c) PVP.

The volcanic ash used in this study was obtained from the Jilin Province of China. The chemical

composition of the volcanic ash is shown in Table 2. It can be seen that the sum proportion of SiO_2 and Al_2O_3

is more than 50%. The XRD pattern of the volcanic ash shown in Figure 2 indicates that the amorphous and

feldspar-like minerals are the main phase of volcanic ash. The particle size distribution of volcanic ash is

shown in Figure 3. As can be seen, d_{10}, d_{50} and d_{90} of volcanic ash are 1.230, 13.289 and 57.195 μm,

respectively.

110

Table 2 Chemical composition of volcanic ash (wt%).

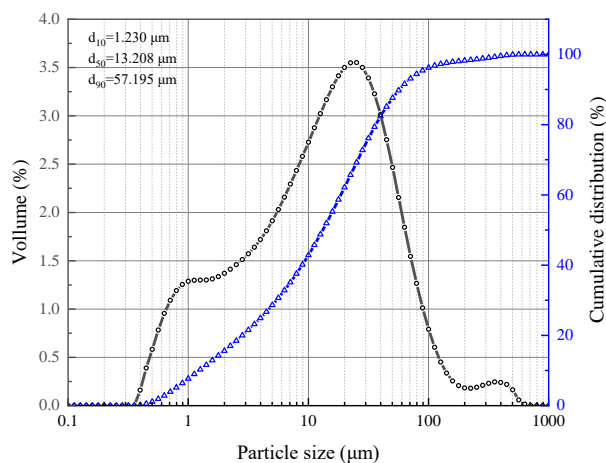| Item	SiO$_2$	FeO	Al$_2$O$_3$	CaO	Na$_2$O	K$_2$O	MgO	TiO$_2$	P$_2$O$_5$	MnO
Volcanic ash	43.3	16.7	16.5	8.8	3.8	3.3	3.0	2.9	0.7	0.3

111
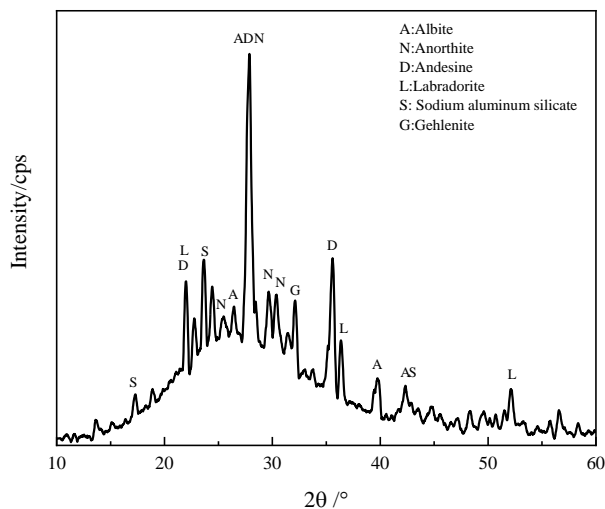
112

113

Figure 2 XRD pattern of volcanic ash.

114

115

Figure 3 Particle size distribution curves of volcanic ash.

116   The alkali activator used was NaOH solution, prepared by mixing NaOH pellets with 99% purity (Beijing

117   Chemical Works, Beijing, China) with distilled water.

118   **2.2 Methods**

119   **2.2.1 Preparation of CNF dispersions**

120   CNFs were ground with a mortar (bowl for grinding) to destroy the fluffy structure produced by the lap

121   between fibers. Then, the dispersions testing for the effect of surfactant type, dosage, and ultrasonic time was

122   prepared, as shown in Table 3.

For the effect of surfactant type tests, the concentration of CNFs was constant at 2 g/L using MC, PC, and PVP as surfactants, and a control group without surfactants was set. The mass ratio of surfactant/CNFs was fixed at 6:1. The detailed procedure included weighing surfactants and CNFs, dissolving the surfactants into distilled water and stirring manually for 3 min, adding CNFs to the surfactant solution, and mixing for another 2 min. Then, the suspension was dispersed in an ultrasonic crusher (Sonics and Materials Vibra-Cell VCX800, USA) for 30 min with an amplitude of 80% at the cycle of 15 s and a temperature limit of 60°C to prevent flocculation of the surfactant due to overheating. The resulting dispersions were the CNF-aqueous solution, and the CNF-alkali solution was obtained after adding 8 mol/L NaOH solution. The control and experimental groups were denoted N-W, MC, PC, and PVP for the CNF-aqueous solution and N-Na, MC-Na, PC-Na, and PVP-Na for the CNF-alkali solution, respectively.

PC was chosen as the only surfactant for the effect of surfactant dosage tests, and the mass ratio of surfactant/CNFs was set at 4:1, 6:1, 8:1, and 10:1. The rest of the test conditions and procedures remained unchanged. The CNF-aqueous solutions were denoted PC4, PC6, PC8, and PC10, and the CNF-alkali solutions were marked PC4-Na, PC6-Na, PC8-Na, and PC10-Na.

The effect of ultrasonic time of 0 min, 15 min, 30 min, and 60 min was also compared at the mass ratio of surfactant/CNFs at 6:1 using PC as the surfactant. The CNF-aqueous solutions were denoted PC-0, PC-15, PC-30, and PC-60, and the CNF-alkali solutions were denoted PC-0-Na, PC-15-Na, PC-30-Na, and PC-60-Na.

Table 3 Dispersion test schemes.

Testing groups	Surfactant type	The mass ratio of surfactant/ CNFs	Ultrasonic time (min)	Aqueous or NaOH solution
N-W	/	/	30	Aqueous
N-Na	/	/	30	NaOH
MC	MC	6:1	30	Aqueous
MC-Na	MC	6:1	30	NaOH
PC4	PC	4:1	30	Aqueous
PC4-Na	PC	4:1	30	NaOH
PC-0	PC	6:1	0	Aqueous
PC-0-Na	PC	6:1	0	NaOH
PC-15	PC	6:1	15	Aqueous
PC-15-Na	PC	6:1	15	NaOH
PC	PC	6:1	30	Aqueous
PC-Na	PC	6:1	30	NaOH
PC-60	PC	6:1	60	Aqueous

PC-60-Na	PC	6:1	60	NaOH
PC8	PC	8:1	30	Aqueous
PC8-Na	PC	8:1	30	NaOH
PC10	PC	10:1	30	Aqueous
PC10-Na	PC	10:1	30	NaOH
PVP	PVP	6:1	30	Aqueous
PVP-Na	PVP	6:1	30	NaOH

142

2.2.2 Characterization of CNFs dispersion

143

144 The dispersion uniformity and proportion of CNF aggregations in aqueous and alkali solutions were

145 comparatively evaluated by a developed quantitative characterization method for microscope image

146 processing.

147 Firstly, the microscope images were obtained by the following steps: 1. Placed 10 drops sampled from

148 the mid-position of the CNF solution on glass slides using a pipetting gun and cover them with coverslips. 2.

149 Waited for 3-5 min for the particles to settle. 3. Took 50 images randomly of the drops from each group of

150 dispersions at a magnification of 160× using a microscope (VR-3200, Keyence, Japan).

151 Then, all the acquired images were processed with a developed program based on OpenCV to identify,

152 binarize, and analyze CNF aggregations' size and number. The maximum inter-class variance (OTSU) method

153 was used to calculate the global threshold and accurately binarize the images to reflect the aggregation

154 morphology. The calculation principle is shown in Equations (1) and (2).
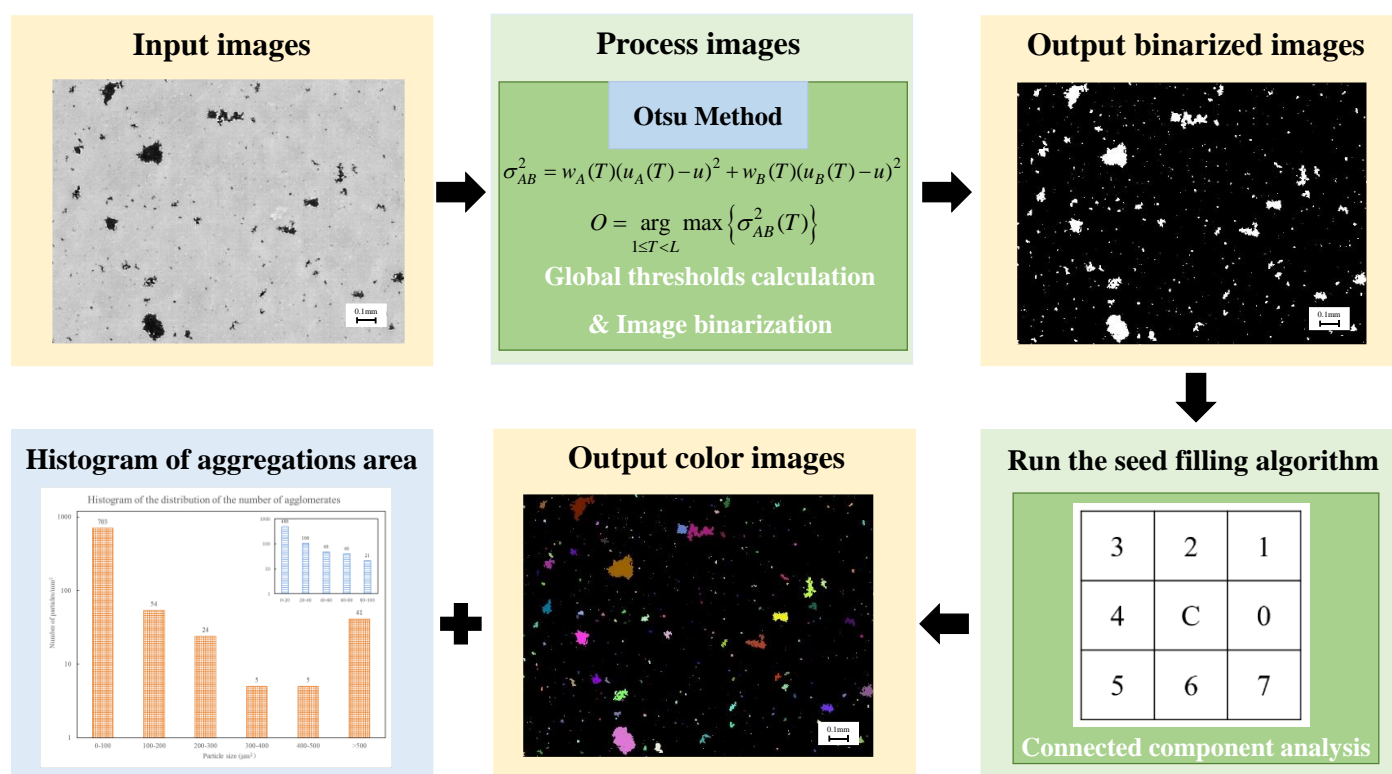
155
$$\sigma_{AB}^2 = w_A(T)(u_A(T)-u)^2 + w_B(T)(u_B(T)-u)^2 \tag{1}$$

156
$$O = \underset{1 \le T < L}{\arg\ \max}\left\{\sigma_{AB}^2(T)\right\} \tag{2}$$

157 Where σ_{AB}^2 is intra-class variance; A and B are the set of pixel points in the foreground and background

158 areas; L is the grayscale value; T is the segmentation threshold; w_A and u_A are the proportion of foreground

159 points to the image and the average grayscale; w_B and u_B are the proportion of background points to the image

160 and the average grayscale; u is the average grayscale value of the whole image, and O is the best threshold

161 value to be used in the end. The program also supports manual input of specified thresholds to adjust the image.

162 After the binarization processing, the connected domain of the image was analyzed by the seed filling

163 method to determine the areas that have the same grey value and are adjacent to each other. Information about

164 the connected domains in the foreground can be obtained and automatically output in the form of color maps

165 and tables. The tables included the area of each aggregation, the total number of aggregations, and the

proportion of the agglomerate area in the whole image. Based on this, the distribution of different aggregation

areas per mm^2 can be calculated and used as an indicator, together with the area proportion, for quantitative

evaluation of the dispersion effect of CNF. Figure 4 presents the flow chart of the scheme for image processing.

Input images

Process images

Otsu Method

$$\sigma_{AB}^2 = w_A(T)(u_A(T)-u)^2 + w_B(T)(u_B(T)-u)^2$$

$$O = \underset{1 \le T < L}{\arg\max}\left\{\sigma_{AB}^2(T)\right\}$$

Global thresholds calculation

& Image binarization

Output binarized images

Histogram of aggregations area

Histogram of the distribution of the number of agglomerates

Output color images

Run the seed filling algorithm

3	2	1
4	C	0
5	6	7

Connected component analysis

Figure 4 Scheme flow chart for image processing.

The zeta potential of the dispersions was characterized by an analyzer (Zetasizer Nano ZS90, Malvern,

UK) to investigate the dispersion mechanism. The dispersions were diluted 20 times before testing to keep the

measured values within the test range.

In addition, the stability of dispersions after 0 h, 12 h, and 72 h ultrasonication was assessed by visual

observation of the status and precipitation.

2.2.3 Synthesis of nanocomposites of CNF and geopolymer

Four CNF/geopolymer nanocomposites with 0 and 0.1% CNFs by weight of volcanic ash were prepared

to test the mechanical properties and microstructure, denoting F0 and F10. The content of 0.1 wt% was chosen

because it was determined that 0.1 wt% of nanofibers could effectively reinforce the cementitious materials,

while the effect would be negatively affected below or above the content (Al-Rub et al., 2012; Ge et al., 2015;

Li et al., 2021; Rovnaník et al., 2016). The NaOH solution was prepared 24 h before casting at a constant

concentration of 8 mol/L, and the water/binder ratio was 0.30 for all groups. The volcanic ash and CNF

dispersions were pre-mixed for 60 s in a mortar mixer (DB-10, Jianyi, Jiangsu, China) to reduce the direct

184   contact between CNF and NaOH. Then the NaOH solution was added and stirred at 140±5 r/min for 120 s and

185   285±10 r/min for another 120 s to obtain the geopolymer nanocomposites. The slurry was then poured into

186   molds of $40 \times 40 \times 160$ mm^3 and vibrated. The molds were covered by polyethylene film and cured at 60 °C.

187   After 6 h, the specimen was demolded and placed in the curing box at 60 °C at 80% relative humidity for 3,

188   7, and 28 days to avoid shrinkage and efflorescence (Jiang et al., 2023).

189   **2.2.4 Characterization of nanocomposites of CNF and geopolymer**

190   According to GB/T-17671-2020, the three-point bending and uniaxial compression tests were carried out

191   using the improved electronic universal testing machine (RGM-6300, Shenzhen Regel Instrument, China) for

192   3, 7, and 28 days. Three specimens were tested for flexural strength with a 0.1 mm/min displacement rate, and

193   the span was 100 mm. The compressive strength test was conducted on the two halves of the prism obtained

194   from three-point bending tests with a 0.5 mm/min displacement rate.

195   To evaluate the changes in microscopic morphology and pore structure of the geopolymer after the

196   addition of CNF and to verify the enhancement effect of dispersed CNF, the microscopic morphology and C-

197   element distribution were characterized by SEM-EDS (SU8020, Hitachi, Japan). The pore size distribution

198   and porosity of the geopolymer nanocomposites were evaluated by MIP (Autopore IV 9500, Micromeritics

199   Instrument, Norcross, Georgia).

200   **3.Results and discussion**

201   **3.1 Dispersion effect of CNFs in solutions**

202   **3.1.1 Effect of surfactant type**

203   (1) Microscopic image processing analysis

204   Typical optical micrographs, binary images, and histograms of the area distribution of CNF aggregations

205   in aqueous solutions obtained from microscopic image processing are shown in Figure 5. As CNFs floated

206   completely on the aqueous surface without surfactant and could not be tested, the control group of N-W was

207   not included in this part. It can be seen from the macroscopic state in Figure 5 that all three types of surfactants

208   were beneficial to the dispersion of CNFs in aqueous. No notable large particles were in the images, and the

209   distribution seemed uniform as point-like aggregations. As shown in the histogram of area distribution, the

210   area of CNF aggregations was concentrated in the range of 0-100 μm^2, with the proportion of MC, PC, and

211   PVP being 99%, 98%, and 99%, respectively. The numbers of aggregations >100 μm^2 were all below 3%.

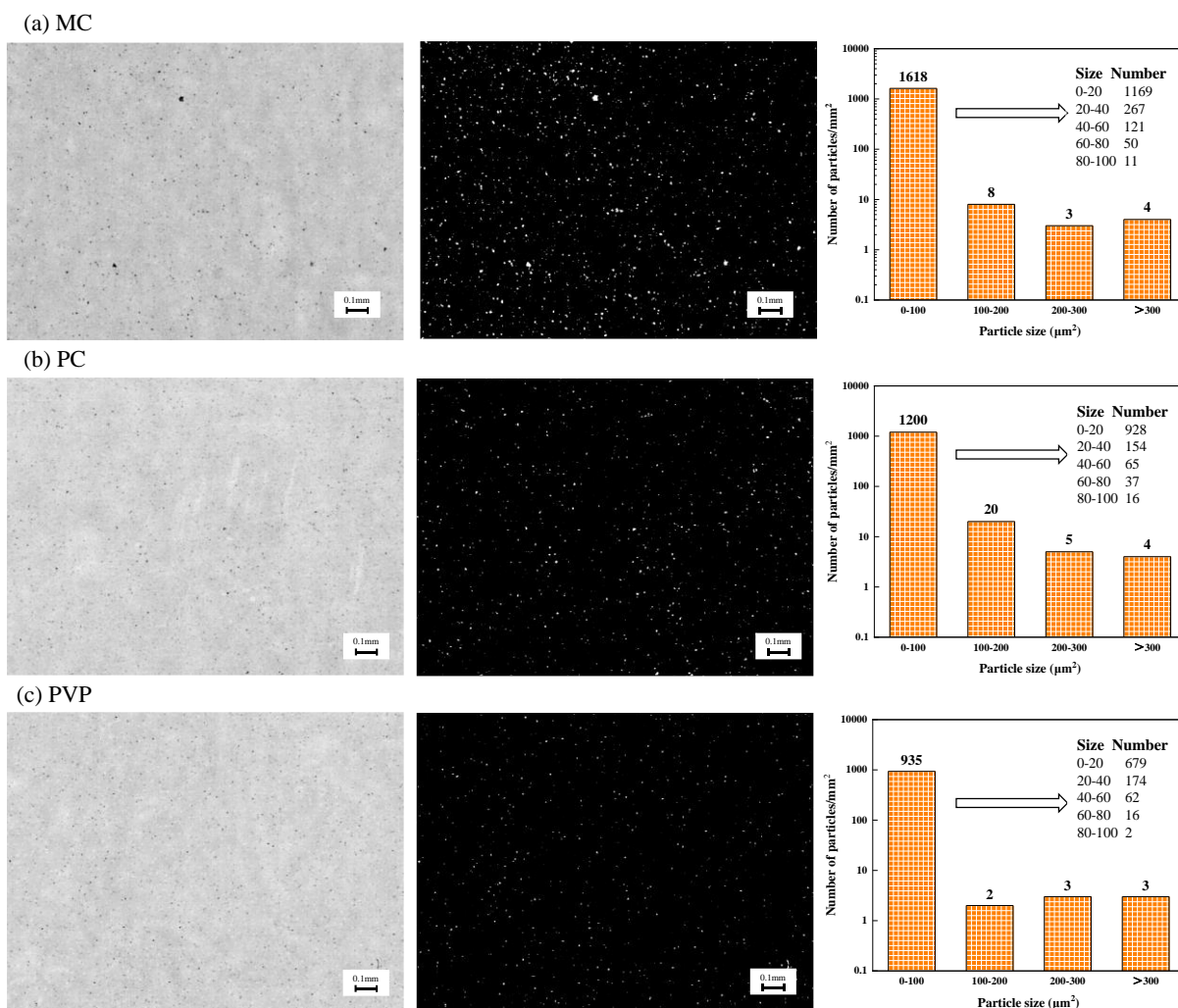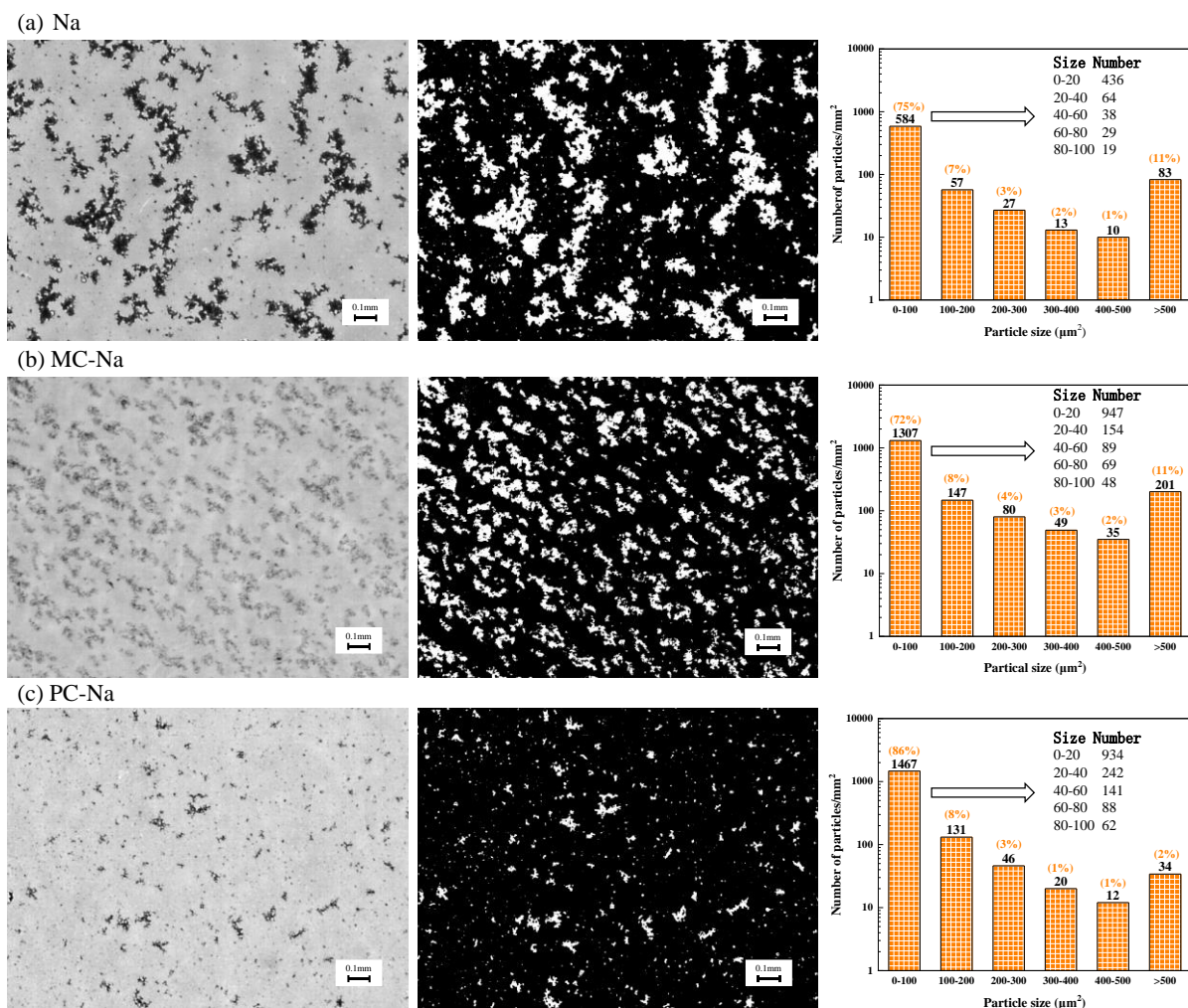212   Thus, all dispersions were considered high-quality.

Figure 5 Typical optical micrographs (160×), binary images, and histograms of the number of CNF particles per mm^2 versus the area of the particles of each area class in aqueous solutions with (a) MC, (b) PC, and (c) PVP.

Typical optical micrographs, binary images, and histograms of the area distribution of CNF aggregations in alkali solutions obtained from microscopic image processing are presented in Figure 6. It was noted that CNFs in the PVP-Na group agglomerated rapidly and exhibited an apparently oversized particle that cannot be included in the magnification of 160×. The optical micrograph (40×) of the large aggregation formed is displayed in Figure 7. Therefore, we believe that PVP does not disperse CNF well in NaOH, and PVP-Na is no longer involved in the comparison. Comparing the morphology shown, the Na group without surfactant formed aggregations with irregular shapes and various sizes, and large particles can be observed. The MC-Na group showed flocculent particles of similar size, clearly different from the other groups. Particles in PC-Na seemed to be smaller in different shapes. The histogram of area distribution indicated that the area of aggregations in the CNF-alkali solution was still the most in the 0-100 μm^2 interval, but the proportion of which was significantly lower than that of the corresponding aqueous solution. The number of aggregations

227 in the Na, MC-Na and PC-Na groups accounted for 75%, 72% and 86% of the total. >500 μm^2 aggregations

228 were 11%, 1%, and 2% of the total in Na, MC-Na and PC-Na groups, respectively. The significant increase of

229 aggregations >100 μm^2 mainly came from the particles already present in the aqueous and the secondary

230 agglomeration of CNFs in the alkaline solution (Stephens et al., 2016).

231

232 Figure 6 Typical optical micrographs (160×), binary images and histograms of the number of CNF particles per mm^2 versus the

233 area of the particles of each area class in (a) NaOH, (b) MC-Na, and (c) PC-Na solutions.
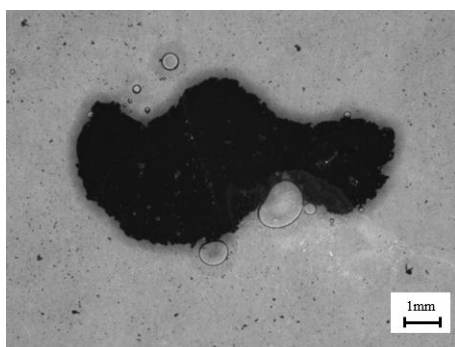
234

235 Figure 7 The optical micrograph (40×) of the large aggregation formed in the PVP-Na group.

236 Table 4 lists the relevant parameters for the aggregation area calculated. The total aggregations in MC,

237 PC, and PVP groups were 1632, 1225, and 941, respectively. The MC group had the most significant particle

238 proportion of 1.08% of the total image area, while the PC and PVP groups were 0.89% and 0.64%, respectively.

239 In terms of the average size of the aggregations, the results were basically the same for the three groups. The

240 number of aggregations >1000 μm^2 could be ignored, and the maximum particle size for all groups was around

241 2200 μm^2, with only a 35 μm^2 difference between the most significant MC and the minor PVP groups. Overall,

242 all three surfactants effectively dispersed CNFs in aqueous, with PVP performing outstanding, followed by

243 PC and MC.

244   For CNF-alkali solutions, Table 4 shows that the total number of aggregations was comparable, between

245 1710 and 1820, except for the Na group, with only 774. The proportion of aggregation area to the whole image

246 in the MC-Na group reached 18.84%, exceeding 13.84% in the Na and 4.83% for PC-Na groups. Three groups

247 displayed remarkably different average particle sizes, with 571 μm^2 in the Na group and only 87 μm^2 in PC-

248 Na. The number of particles >1000 μm^2 in the MC-Na group was up to 113, while the PC-Na group had only

249 14. The largest aggregation size that could be detected exceeded 30,000 μm^2 for both the Na and MC-Na

250 groups and 7345 μm^2 for PC-Na. Therefore, it was believed that the well-performed surfactants in aqueous

251 would fail in a strong alkali solution, with notable aggregations of CNFs.

252   Table 4 CNF particle size analysis in aqueous and alkali solutions with different surfactants.

	MC	PC	PVP	Na	MC-Na	PC-Na
Total number of particles/mm^2	1632	1225	941	774	1819	1710
Total particle area proportion (%)	1.08	0.89	0.64	13.84	18.84	4.83
Average particle size (μm^2)	21	20	20	571	325	87
Number of particles ＞1000 μm^2	0	1	1	60	113	14
Maximum particle size (μm^2)	2230	2215	2195	32693	30598	7345

253

254   (2) Dispersion mechanisms

255   According to the Derjagin-Landau-Verwey-Overbeek (DLVO) theory, surfactant molecules adsorbed on

256 CNF provide repulsive interaction that reduces the surface tension of the dispersion and prevents aggregations

257 (Liebscher et al., 2016; Motoyoshi et al., 2022; WANG et al., 2012). The adsorption effect can be characterized

258 by zeta potential, and the larger the absolute value of zeta potential, the greater the repulsive interaction to

259 overcome the van der Waals forces. Table 5 shows the zeta potential of CNF-aqueous and CNF-alkali solutions.

260 PVP presented the highest zeta potential at -12.0 mV, followed by PC at -9.6 mV and MC at -1.8 mV. It can

261 be inferred that although the surfactants used had different structures, they all can produce repulsive forces in

262   aqueous, but the effects were not stable enough since the zeta potentials were below 25 mV.

263   For CNF-alkali solutions, it can be found that the difference in zeta potential between the groups is

264   noticeable. Na showed electronegativity at -14.9 mV, and MC-Na, PC-Na, and PVP-Na turned to low values

265   for different degrees, at -5.0, -4.0, and -5.6 mV, respectively, proving the adsorption of surfactant molecules.

266   PC-Na significantly changed zeta potential and outperformed MC-Na and PVP-Na, benefiting from the comb-

267   like structure consisting of polymeric main chains and side chains. MC and PVP with simple structures

268   overcome van der Waals forces mainly by forming molecular films on the CNFs surface, and PC can adjust

269   the chain of adsorption depending on the environment. As shown in Figure 8, in alkali solutions, Na^+ from

270   high alkalinity activators may replace the surfactant molecules and adsorbed directly onto the CNFs, resulting

271   in partial stripping of the surfactants and a rapid decrease in the zeta potential of the slipping layer in the

272   double layer repulsion. The van der Waals gravitational potential energy was not affected, thus severely

273   shielding the interaction between charges or spatial site resistances, leading to re-aggregations of CNFs (Lu

274   and Zhong, 2022; Lu et al., 2018). PC molecules with a comb-like structure were attached to the CNFs surface

275   with side chains when pH>11 to inhibit the proximity of some Na^+ and kept the slipping surface away, resulting

276   in an abruptly positive change of zeta potential due to the adsorption of Na^+ on the main chain(Zhao et al.,

277   2018). The adsorption effect was proposed to be related to the molecular weight of the side chains (Liebscher

278   et al., 2016; Qin et al., 2021). Therefore, the repulsion between CNFs wrapped by PC molecules was superior

279   to MC and PVP, and the variation of zeta potential was more significant.

280

Table 5 Zeta potential of CNF-aqueous and CNF-alkali solutions.

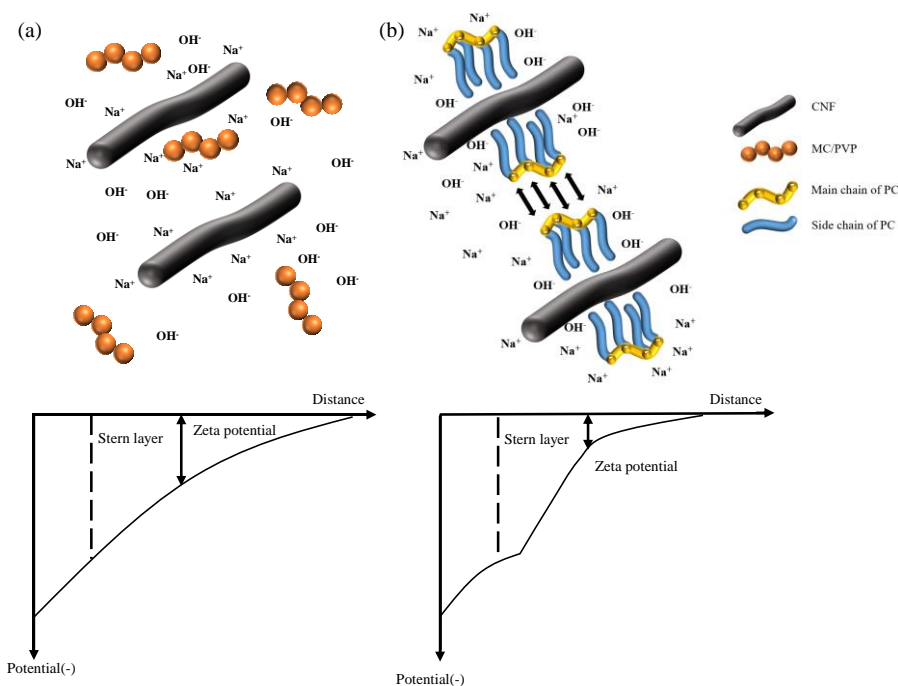|	MC	PC	PVP	Na	MC-Na	PC-Na	PVP-Na
Zeta potential (mV)	-1.8	-9.6	-12.0	-14.9	-5.0	-4.0	-5.6

281

Figure 8 Schematic diagram of CNF dispersion mechanisms and double electric layers in (a)MC-Na/PVP-Na and (b)PC-Na.
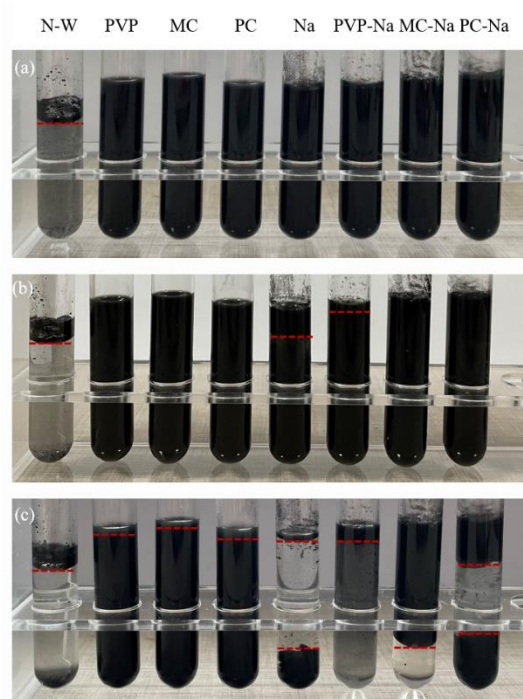
(3) State and stability

Figure 9 shows visual observations of the dispersion state and stability of the CNFs in aqueous and alkali solutions at 0 h, 12 h, and 72 h after ultrasonication. The CNFs were difficult to dissolve in aqueous in the N-W group without surfactant and floated on the surface, partially sucking on the wall of the tubes. Over time, the solution became clarified since the limited dissolved CNFs moved up. MC, PC, and PVP groups displayed homogeneous black solutions at 0 h and 12 h, with slight stratification at 72 h as the CNFs settled. Overall, the dispersion state of CNF-aqueous solutions remained satisfactory and stable for 72 h.

CNFs in alkali solutions behaved much less well than in aqueous. CNFs in the Na group without surfactant suspended in the solution as uneven. Stratification occurred at 12 h, with some CNFs aggregates upwards and some downwards, with the middle gradually becoming transparent, and by 72 h, the boundaries of the three layers were visible. Surfactants alleviated the phenomenon at 12 h. The MC-Na and PC-Na groups presented uniformly black, and the PVP-Na group was slightly stratified due to the production of large aggregations. However, all groups had clear boundaries at 72 h, indicating poor long-term stability. The difference was that the aggregations in MC-Na and PVP-Na were concentrated above the solution. The former contained a considerably larger volume of the CNF particles than the clear solution, while the latter behaved the opposite. The aggregations in PC-Na were truncated from the middle and divided into three layers, like Na. The probable reason for the change in dispersion state was that Na^+ adsorbed on the CNF surface and the

surfactant molecules gradually flaked off. Thus, the spatial site resistance or the electrostatic repulsion decreased, resulting in a certain amount of aggregations. Moreover, once aggregations were formed, the specific surface area of the exposed CNFs decreased dramatically, leading to the desorption of the surfactants, further intensifying the agglomerations and creating a vicious cycle (Zhao et al., 2018). As a result, maintaining the stability of the dispersions was challenging. The different layering behaviors may be related to the plastic viscosity of the solution. The CNFs in PC-Na and Na lacked the force to converge in the same direction since the relatively low plastic viscosity, thus splitting into three layers, while MC had.

The above analysis concluded that PC effectively dispersed CNFs in aqueous and was superior to MC and PVP in alkali solutions, so PC was selected as the surfactant for the subsequent tests.


Figure 9 Dispersion state and stability of CNFs in aqueous and alkali solutions at (a) 0h, (b) 12h, and (c) 72h after ultrasonication.

3.1.2 Effect of surfactant dosage

Figure 10 shows typical optical micrographs and distribution of aggregations in CNF-aqueous solutions prepared with PC to CNFs mass ratios of 4:1, 6:1, 8:1, and 10:1. It can be seen from Figure 10 (a)-(d) that the optimal dosage was PC6 in CNF-aqueous with no noticeable particles and uniform distribution. Figure 10 (e) presented that all groups' total aggregations were between 1200 and 1400. 98% of the particles in PC6 were in the range of 0-100 μm^2, while PC4, PC8, and PC10 had 94%, 94%, and 93% of this zone. It can be explained that PC4 had insufficient molecules to adsorb on CNFs, resulting in small particles. In PC8 and PC10, the adsorption was saturated, and the excess molecules may increase the plastic viscosity, affecting the

consequence. Given that the aggregation size of all groups was more than 90% concentrated in 0-100 μm^2, it was considered that the dispersion was successful in all cases.
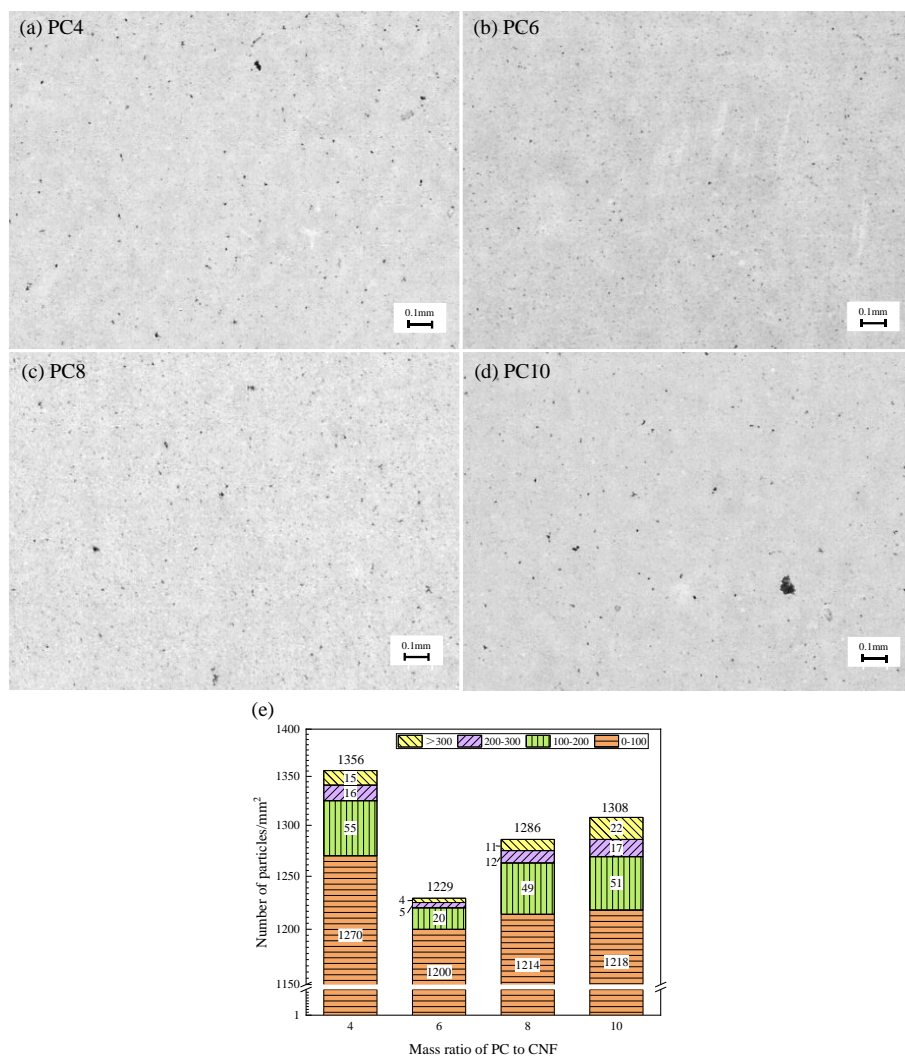
Figure 10 Typical optical micrographs (160×) of (a) PC4, (B) PC6, (c) PC8, and (d) PC10 solutions, and (e) distribution of CNF particles per mm^2 in each group.

Typical optical micrographs and distribution of aggregations in CNF-alkali solutions are shown in Figure 11. It can be found that aggregates formed in the NaOH solutions regardless of the PC dosage. The size of the particles in PC4-Na, PC6-Na, and PC8-Na was similar in size and uniformly dispersed, while PC10-Na appeared as relatively larger particles. Figure 11 (e) revealed that the total aggregations increased compared to the aqueous solution between 1500 and 1800. 82%, 86%, 86%, and 80% of PC4-Na, PC6-Na, PC8-Na, and PC10-Na particles were in the 0-100 μm^2 size range, and the number of particles >500 μm^2 increased compared to aqueous, accounting for 5%, 2%, 3% and 4% of the total, respectively. It was clear that PC6-Na and PC8-Na were well-dispersed.
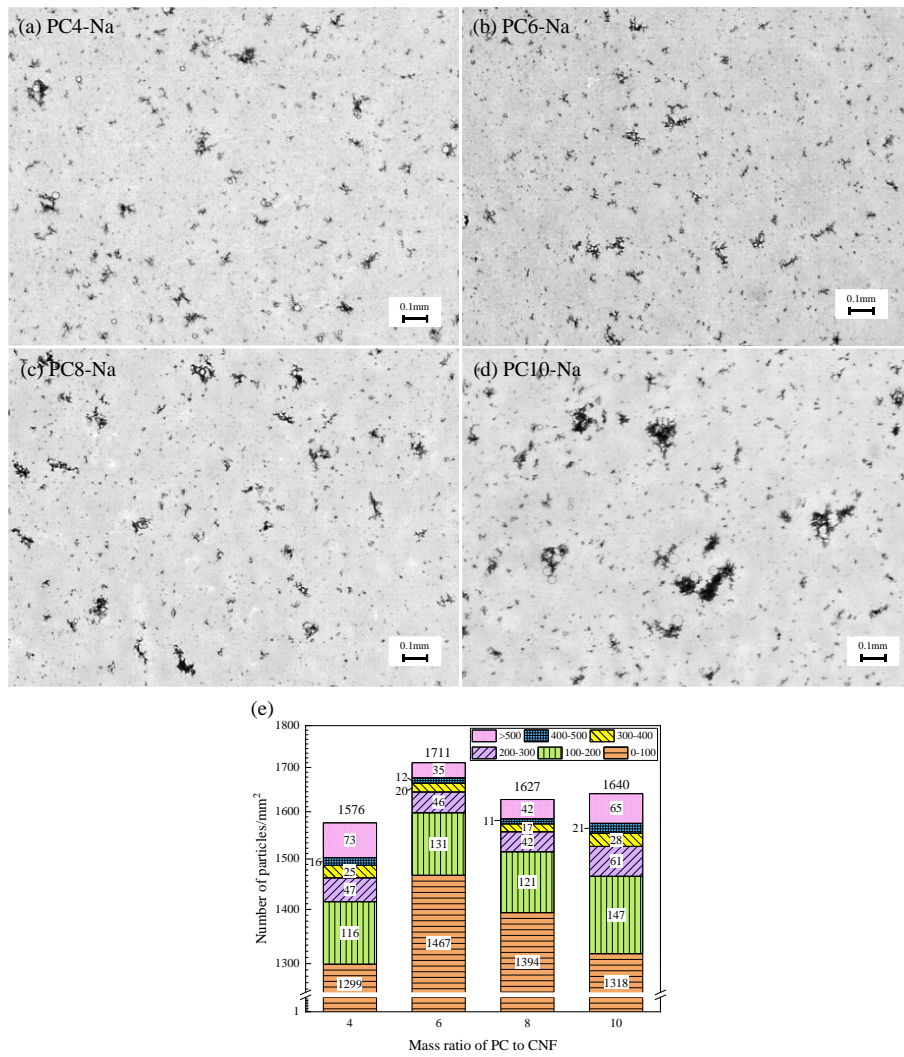
Figure 11 Typical optical micrographs (160×) of (a) PC4-Na, (b) PC6-Na, (c) PC8-Na, and (d) PC10-Na solutions, and (e)

distribution of CNF particles per mm^2 in each group.

Table 6 lists the relevant parameters for the aggregation area calculated. The PC10 group showed the most significant proportion of aggregations at 1.71%, PC4 and PC8 were comparable at 1.38% and 1.18%, and PC6 was at 0.89%. The average size of aggregations and the maximum size of the four groups showed the same pattern, PC10>PC4>PC8>PC6. For aggregations >1000 μm^2, the numbers were below 5 in all groups, and the maximum particle size was about 2300 except for PC10 exceeding 3000. Table 6 also shows that in the CNF-alkali solutions, the proportion of aggregations increased by 4-5 times compared to that in the aqueous solution. The minor proportion was 4.83% for PC6-Na, and the largest was 6.59% for PC4-Na. The average size of the particles ranged from 87 μm^2 to 130 μm^2, and the PC6-Na and PC8-Na groups still performed better. Aggregates >1000 μm^2 reached more than 30 in the PC4-Na and PC10-Na groups, while neither the PC6-Na nor PC8-Na groups had more than 20. The maximum size appeared in PC10-Na with

346 13,438 μm[2,] and PC6-Na was about half of it with 7,345 μm^2. The conclusion could be drawn from the

347 comparison that the dosage of PC improved the dispersion of CNFs in the alkali solution slightly. Still, the

348 effect was superior at 6:1, so this dosage of PC was adopted for subsequent tests.

349 Table 6 CNF particle size analysis in aqueous and alkali solutions with different PC dosages.

	PC4	PC6	PC8	PC10	PC4-Na	PC6-Na	PC8-Na	PC10-Na
Total particle area proportion (%)	1.38	0.89	1.18	1.71	6.59	4.83	5.70	6.21
Average particle size (μm^2）	31	22	28	40	128	87	90	130
Number of particles ＞1000μm^2	2	1	2	5	35	14	20	30
Max particle size (μm^2）	2454	2300	2349	3145	10721	7345	13278	13438

350

351 **3.1.3 Effect of ultrasonic time**

352 Typical optical micrographs and distribution of aggregations in CNF-aqueous solutions with 0 min, 15

353 min, 30 min, and 60 min ultrasonication are presented in Figure 12. Comparing Figure 12 (a)-(d), it was

354 evident that ultrasonication was highly beneficial to the dispersion of CNFs in aqueous. Aggregations in

355 various scales co-existed in the PC-0 group, some of the large ones were broken up after 15 min ultrasonication

356 of PC-15, and there were no apparent agglomerates in PC-30 and PC-60. It can be seen in Figure 12 (e) that

357 the number of particles in PC-0 was small, but only 83% of particles were in the range of 0-100 μm^2 and 6%

358 of >300 μm^2. After ultrasonication, the total number was between 1200 and 1300. The 0-100 μm^2 proportion

359 increased with the ultrasonic time, showing 85%, 97%, and 99% for PC-15, PC-30, and PC-60, respectively,

360 while the proportion of >300 μm^2 gradually decreased.

361 Figure 13 depicts typical optical micrographs and the distribution of aggregations in CNF-alkali solutions.

362 The aggregations were more pronounced in the alkaline solution than in the aqueous solution and tended to

363 decrease in size with increasing sonication time. As shown in Figure 13 (e), the total number of aggregations

364 increased, and at the same time, the proportion of large agglomerates became less with ultrasonic time. The

365 proportion of particles of 0-100 μm^2 was 83%, 83%, 86%, and 86% for PC-0, PC-15, PC-30, and PC-60

366 groups, respectively, while the proportion of >500 μm^2 was 3%, 3%, 2%, and 1%, respectively. It can be

367 revealed that the ultrasonic time slightly improved the dispersion of CNF in the alkaline solution, unlike in

368 the aqueous.

(a) PC-0

(b) PC-15

(c) PC-30

(d) PC-60

(e)
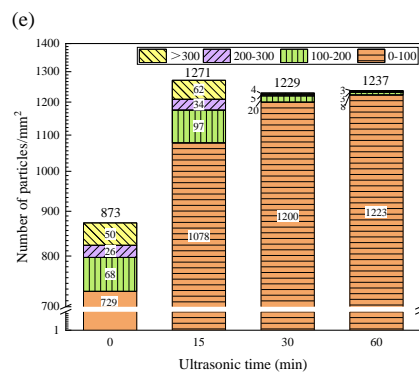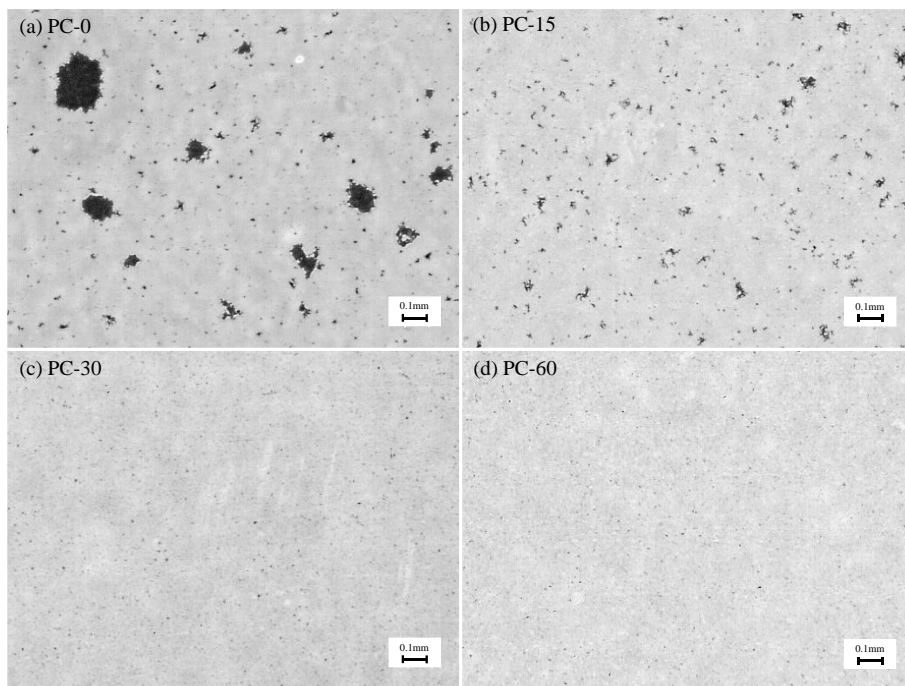
Figure 12 Typical optical micrographs (160×) of CNF aqueous solutions with (a) 0 min, (b) 15 min, (c) 30 min, and (d) 60 min ultrasonic processing, and (e) distribution of CNF particles per mm^2 in each group.
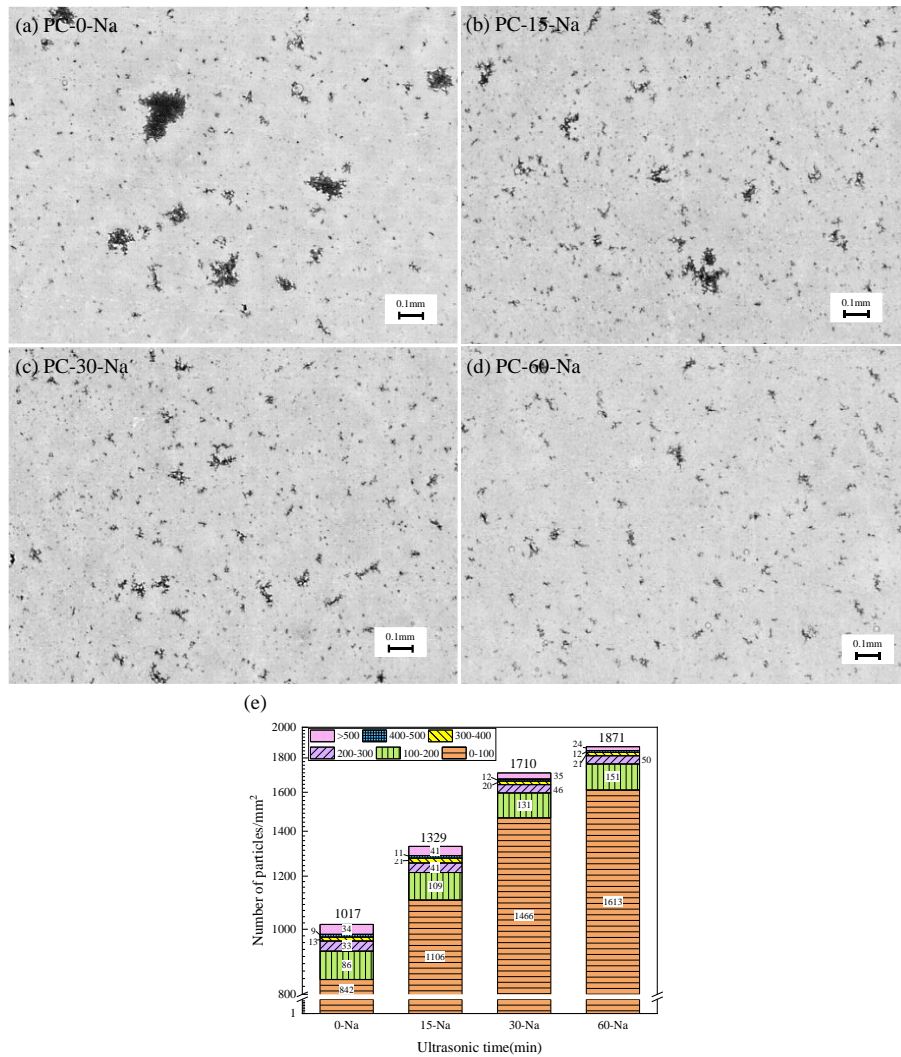
Figure 13 Typical optical micrographs (160×) of CNF alkali solutions with (a) 0 min, (b) 15 min, (c) 30 min, and (d) 60 min

ultrasonic processing, and (e) distribution of CNF particles per mm² in each group.

The relevant parameters for the aggregation area calculated are listed in Table 7. As the ultrasonic time increased from 0 to 60 min, the proportion of aggregation area in the aqueous solutions decreased from 5.32% to 0.83%, and the average size decreased from 181 μm^2 to 20 μm^2. The number of aggregations >1000 μm^2 in PC-0, PC-15, PC-30, and PC-60 was 20, 14, 1, and 1, respectively, and the maximum size was also reduced from 40,368 μm^2 to 2,228 μm^2. It should be noted that the results obtained for PC-30 and PC-60 were almost identical, proving that the ultrasound energy for 30 min was sufficient to break up the agglomerated CNFs, and a further increase in time had no longer significant benefit. Also, it has been suggested that long ultrasonic time reduces the aspect ratio of CNFs, thus reducing their enhancement effect (Metaxa et al., 2013). For alkali solutions, the proportion of aggregation area decreased from 6.42% to less than 5% with ultrasonic time. At the same time, the average particle size was reduced by 53%, the aggregations >1000 μm^2 were cut from 21

385   to 10, and the maximum size was with 88% reduction. In summary, ultrasonic time somewhat influenced the

386   dispersion of CNFs in the alkali solution. 30 min ultrasonication was comparable to 60 min, so the subsequent

387   experiments would adopt 30 min ultrasonication.

388   Table 7 CNF particle size analysis in aqueous and alkali solutions with different ultrasonic time.

	PC-0	PC-15	PC-30	PC-60	PC-0-Na	PC-15-Na	PC-30-Na	PC-60-Na
Total particle area proportion (%)	5.32	3.46	0.89	0.83	6.42	5.71	4.83	4.68
Average particle size (μm^2)	181	88	22	20	190	103	87	64
Number of particles $>1000\mu m^2$	20	14	1	1	21	17	14	10
Max particle size (μm^2)	40368	4112	2300	2228	45352	14909	7345	5141

389

3.2 Mechanical properties of geopolymer nanocomposites

391   The results of the geopolymer nanocomposites' flexural and compressive strength tested at 3, 7, and 28

392   days are shown in Figure 14. It can be seen from Figure 14 (a) that the flexural strength of F10 reached 3.2

393   MPa at 28 days. The strength was increased by about 30%, 24%, and 23% at 3, 7, and 28 days compared to

394   F0, respectively. The improvement indicated that the well-dispersed CNFs could act as a bridge between

395   microcracks, thus transferring the load with high efficiency to prevent the further development of microcracks

396   and improving flexural strength (Danoglidis et al., 2016; Li et al., 2020).

397   The compressive strength of the geopolymer nanocomposites is shown in Figure 14 (b). F10 also

398   exhibited higher strength than F0 at all ages, and the reinforcement was approximately 21%, 19%, and 16%

399   at 3, 7, and 28 days, respectively. It can be found that the improvement of compressive strength was large at

400   the early stage, which the influence of CNFs on the development of compressive strength can explain. The

401   strength of F0 was 17.0 and 22.0 MPa at 3 and 7 days, respectively, reaching 63% and 81% of that at 28 days.

402   For F10, the strength was 20.5 and 26.1 MPa at 3 and 7 days, respectively, reaching 65% and 83% of 28-d

403   strength. CNFs accelerated the formation of gel products by providing extra nucleation sites at the early stage

404   so that the reinforcement was more considerable (Xu et al., 2021; Zhang et al., 2022). Also, CNFs can act as

405   fillers to refine the cavities, contributing to forming dense microstructures and increasing compressive strength
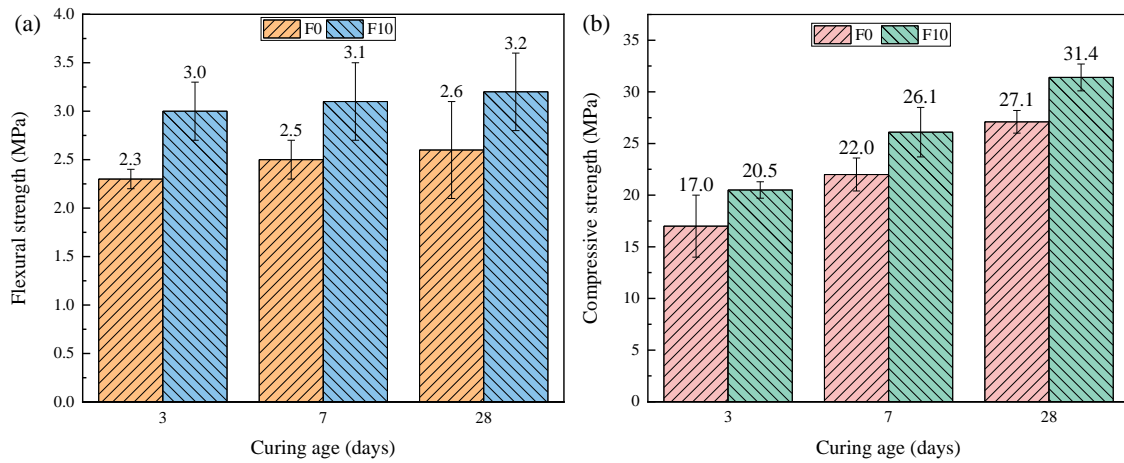
406   (Wang, Q. et al., 2021).

Figure 14 Test results of (a) flexural strength and (b) compressive strength of F0 and F10 geopolymer nanocomposites at 3, 7 and

28 days.

3.3 Microstructural Analysis

3.3.1 Scanning Electron Microscopy coupled with Energy Dispersive Spectroscopy

Tests of element C distribution were carried out using SEM-EDS to confirm the dispersion of CNFs in the geopolymer nanocomposites(Wang and Zhang, 2014). The results for the F10 group are shown in Figure 15. As seen in Figure 15 (a) and (b), CNFs were presented as individuals and embedded in the geopolymer nanocomposites without aggregations. Also, the CNFs played a prominent bridging role. Figure 15 (c) and (d) shows that element C can be detected and was uniformly distributed. The dark areas mainly originated from the cavities in nanocomposites, and the highlighted parts were CNFs. The results further demonstrated that the dispersion scheme proposed was effective.
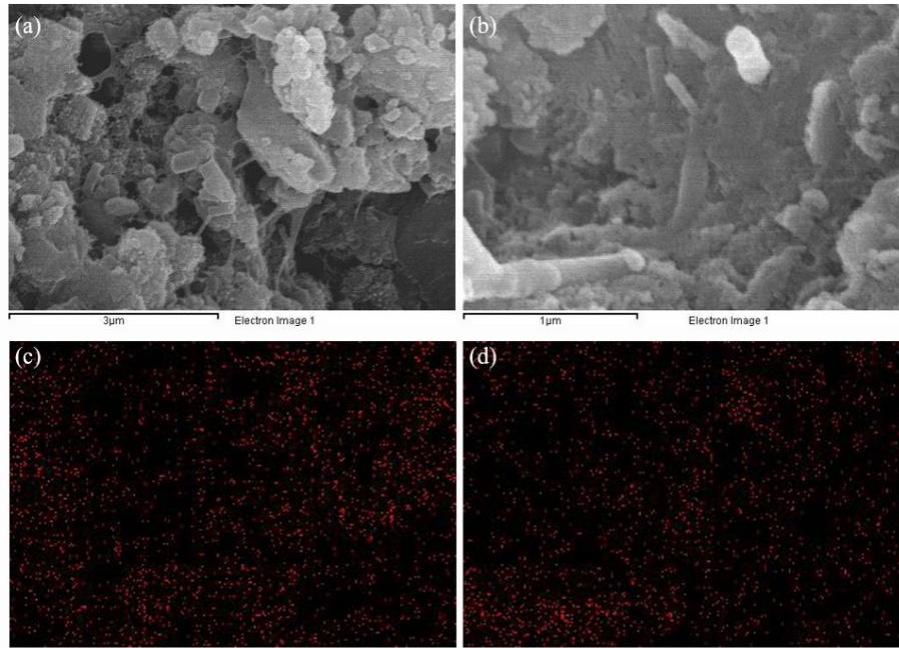
420

421 Figure 15 Typical SEM images of (a) and (b) F10, and EDS mapping of C element in (c) and (d) F10.

422   In addition, typical SEM images of F0 and F10 geopolymer nanocomposites are shown in Figure 16. As

423 shown in Figure 16 (a), the gels generated by the geopolymerization reaction without CNFs were blocky

424 structures of various shapes, accompanied by cavities and microcracks. It can be observed from Figure 16 (b)

425 and (c) that the CNFs were compatible with the geopolymer, bonded effectively by embedding in the gels,

426 filled the cavities, and bridged the products. Also, the nucleation effect was proved to exist since the coated

427 CNFs were found, contributing to the improved microstructure of the nanocomposites (Khater and Abd el

428 Gawaad, 2016), in accordance with the results of strength improvement. Moreover, the holes left by the CNFs

429 pullout were observed in Figure 16 (c), marked with a yellow circle, indicating that CNF increased the energy

430 consumption required for the failure of the geopolymer and modified the mechanical properties.
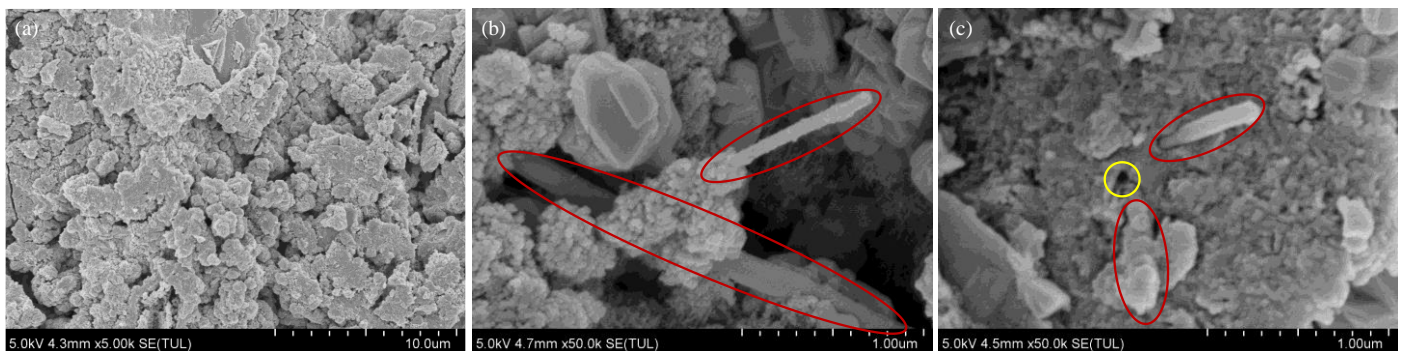

431

432 Figure 16 Typical SEM images: (a) geopolymer without CNF, (b) bonding, filing, and bridging effect, and (c)nucleation and

433 debonding effect in geopolymers with CNF.

3.3.2 Mercury Intrusion Porosimetry

The results of the MIP tests are presented in Figure 17 and Table 8. The curves for F10 can be seen in Figure 17 (a) shifted to the left and tended toward smaller pores. The probable diameter of F0 and F10, represented by the peaks of the curves, were 349.7 and 227.0 nm, respectively. The cumulative intrusion in Figure 17 (b) reflects the porosity. The curve of F10 was almost below that of F0, meaning a decrease in the porosity. Table 8 shows that the total intrusion volume of F0 and F10 was 0.1297 and 0.1074 mL/g, and the average pore diameter of F10 decreased by 33% to 38.73 nm. According to the International Union of Pure and Applied Chemistry (IUPAC), pores <2 nm in diameter are micropores, 2-50 nm are mesopores, and >50 nm are macroporous. The addition of CNFs resulted in an increase in mesopores and a decrease in macropores. The total porosity of F10 was reduced by about 15% relative to F0. It can be concluded that CNFs refined the pore size and modified the pore structure by filling effect to reduce the risk of damage due to defects, reinforcing the compressive strength.
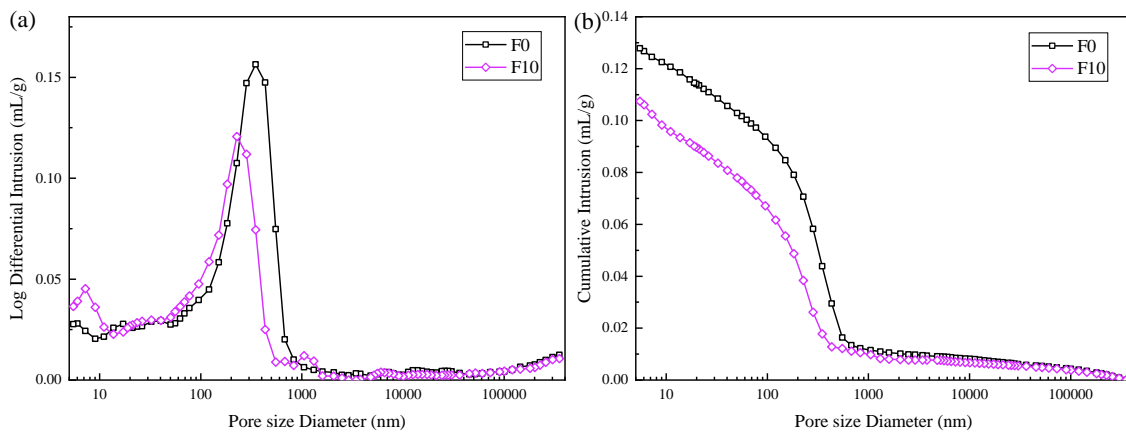

Figure 17 MIP test results for (a) pore size distribution curves and (b) cumulative intrusion curves of F0 and F10.

Table 8 MIP test results of pore size distribution.

Test groups	Total intrusion volume (mL/g)	Average pore diameter (nm)	Mesopores (%)	Macroporous (%)	Porosity (%)
F0	0.1297	57.91	4.21	17.34	21.56
F10	0.1074	38.73	5.01	13.24	18.25

4. Conclusion

In this paper, the CNFs dispersion scheme was preferentially selected by quantitative analysis method of microscopic image processing and zeta potential tests. Then volcanic ash-based geopolymer nanocomposites were prepared. The effect of CNFs on the mechanical properties and microstructure of the nanocomposites

was investigated to promote the massive utilization of volcanic ash and provide an experimental basis for applying CNFs in geopolymers. The following conclusions were obtained:

1. Alkali activators with strong alkalinity and high ionic concentrations lead to severe CNF aggregations and poor dispersion. MC, PC, and PVP performed well in aqueous to disperse CNFs but failed to different degrees in alkali activators. PC was the superior surfactant type to disperse CNFs in alkali solutions. The PC to CNF ratio of 6:1 and 30 min of ultrasonication was the preferred dispersion scheme, with a proportion of aggregation area of 4.83% and an average aggregation area of 87 μm^2.

2. Surfactants failed in alkaline solutions because the high pH affected the adsorption of surfactant molecules on the CNFs' surface, with Na^+ taking its place, weakening the mutual repulsion. The comb-like structure of PC can hinder the approach of some Na^+ since the side chains of PC can attach to the CNFs, resulting in an evident change at zeta potential.

3. 0.1 wt% CNFs could improve the flexural strength by about 30%, 24%, and 23%, and the compressive strength by 21%, 19%, and 16% at 3, 7, and 28 days of the volcanic ash-based geopolymer nanocomposites, proving the reinforcement effect of well-dispersed CNFs.

4. The microstructure of nanocomposites of CNF and geopolymer presented refined pore size and modified pore structures. The average pore size was decreased by 33%, and the porosity was reduced by 15% since CNFs acted as extra nucleation sites, bridged the microcracks, and filled the cavities in geopolymer nanocomposites.

Although volcanic ash-based geopolymer nanocomposites are promising cleaner materials due to the reduction of pollution through the massive use of volcanic ash, this paper still has limitations. The dispersion effect of CNFs was investigated only in alkali activator solutions, but the dispersion in hardened geopolymers was not evaluated since it is difficult to distinguish CNFs from geopolymers directly. Therefore, the discrimination can be improved by introducing new parameters or staining the geopolymer products in the future. In addition, the reinforcement effect was still not as significant as in cement, so surface modification of CNFs would be considered to enhance the compatibility with alkali solutions.

Declaration of Competing Interest

The authors declare that they have no known competing financial interests or personal relationships that could have appeared to influence the work reported in this paper.

484

References

Al-Rub, R.K.A., Tyson, B.M., Yazdanbakhsh, A., Grasley, Z., 2012. Mechanical Properties of Nanocomposite Cement Incorporating Surface-Treated and Untreated Carbon Nanotubes and Carbon Nanofibers. J. of Nanomechanics and Micromechanics. 2(1), 1-6. http://dx.doi.org/10.1061/(ASCE)NM.2153-5477.0000041

Aslani, F., Wang, L., 2019. Fabrication and characterization of an engineered cementitious composite with enhanced fire resistance performance. J. Clean. Prod. 221, 202-214. http://dx.doi.org/10.1016/j.jclepro.2019.02.241

Bai, T., Liu, B., Wu, Y., Huang, W., Wang, H., Xia, Z., 2020. Mechanical properties of metakaolin-based geopolymer with glass fiber reinforcement and vibration preparation. J. Non-Cryst. Solids. 544. http://dx.doi.org/10.1016/j.jnoncrysol.2020.120173

Chuah, S., Li, W., Chen, S.J., Sanjayan, J.G., Duan, W.H., 2018. Investigation on dispersion of graphene oxide in cement composite using different surfactant treatments. Construct. Build. Mater. 161, 519-527. http://dx.doi.org/10.1016/j.conbuildmat.2017.11.154

Danoglidis, P.A., Konsta-Gdoutos, M.S., Gdoutos, E.E., Shah, S.P., 2016. Strength, energy absorption capability and self-sensing properties of multifunctional carbon nanotube reinforced mortars. Construct. Build. Mater. 120, 265-274. http://dx.doi.org/10.1016/j.conbuildmat.2016.05.049

Davoodabadi, M., Liebscher, M., Hampel, S., Sgarzi, M., Rezaie, A.B., Wolf, D., Cuniberti, G., Mechtcherine, V., Yang, J., 2021. Multi-walled carbon nanotube dispersion methodologies in alkaline media and their influence on mechanical reinforcement of alkali-activated nanocomposites. Compos. B Eng. 209. http://dx.doi.org/10.1016/j.compositesb.2020.108559

Djobo, J.N., Elimbi, A., Tchakoute, H.K., Kumar, S., 2017. Volcanic ash-based geopolymer cements/concretes: the current state of the art and perspectives. Environ. Sci. Pollut. Res. Int. 24(5), 4433-4446.

513   http://dx.doi.org/10.1007/s11356-016-8230-8

514   Djobo, J.N.Y., Stephan, D., 2022. Understanding the binder chemistry, microstructure, and physical properties

515   of volcanic ash phosphate geopolymer binder. J. Am. Ceram. Soc. 105(5), 3226-3237.

516   http://dx.doi.org/10.1111/jace.18333

517   El-Sayed, T.A., Shaheen, Y.B.I., 2020. Flexural performance of recycled wheat straw ash-based geopolymer

518   RC beams and containing recycled steel fiber. Structures 28, 1713-1728.

519   http://dx.doi.org/10.1016/j.istruc.2020.10.013

520   Farhan, K.Z., Johari, M.A.M., Demirboğa, R., 2021. Impact of fiber reinforcements on properties of

521   geopolymer composites: A review. J. Build. Eng. 44. http://dx.doi.org/10.1016/j.jobe.2021.102628

522   Ge, S.K., Zhang, Y., Wang, B.M., Zhu, Y., 2015. Characterisation and simulation of highly dispersed carbon

523   nanofibre-reinforced cement materials. Adv. Cem. Res. 27(1), 11-21.

524   http://dx.doi.org/10.1680/adcr.13.00058

525   Heister, E., Lamprecht, C., Neves, V., Tîlmaciu, C., Datas, L., 2010. Higher dispersion efficacy of

526   functionalized carbon nanotubes in chemical and biological environments. Acs Nano 4(5), 2615-2626.

527   http://dx.doi.org/10.1021/nn100069k

528   Horwell, C.J., Baxter, P.J., 2006. The respiratory health hazards of volcanic ash: a review for volcanic risk

529   mitigation. Bull. Volcanol. 69(1), 1-24. http://dx.doi.org/10.1007/s00445-006-0052-y

530   Jiang, L., Gao, L., Sun, J., 2003. Production of aqueous colloidal dispersions of carbon nanotubes. J. Colloid.

531   Interf. Sci. 260(1), 89-94. http://dx.doi.org/10.1016/s0021-9797(02)00176-5

532   Jiang, X., Zhang, Y., Zhang, Y., Ma, J., Xiao, R., Guo, F., Bai, Y., Huang, B., 2023. Influence of size effect on

533   the properties of slag and waste glass-based geopolymer paste. J. Clean. Prod. 383, 135428.

534   http://dx.doi.org/https://doi.org/10.1016/j.jclepro.2022.135428

535   Kan, L.-l., Wang, W.-s., Liu, W.-d., Wu, M., 2020. Development and characterization of fly ash based PVA

536   fiber reinforced Engineered Geopolymer Composites incorporating metakaolin. Cem. Concr. Compos.

537   108. http://dx.doi.org/10.1016/j.cemconcomp.2020.103521

538   Khater, H.M., Abd el Gawaad, H.A., 2016. Characterization of alkali activated geopolymer mortar doped with

539   MWCNT. Construct. Build. Mater. 102, 329-337. http://dx.doi.org/10.1016/j.conbuildmat.2015.10.121

540   Konsta-Gdoutos, M.S., Metaxa, Z.S., Shah, S.P., 2010. Highly dispersed carbon nanotube reinforced cement

541   based materials. Cem. Concr. Res. 40(7), 1052-1059. http://dx.doi.org/10.1016/j.cemconres.2010.02.015

542   Li, F., Yang, Z., Zheng, A., Li, S., 2021. Properties of modified engineered geopolymer composites
543   incorporating multi-walled carbon Nanotubes(MWCNTs) and granulated blast furnace Slag(GBFS).
544   Ceram. Int. 47(10), 14244-14259. http://dx.doi.org/10.1016/j.ceramint.2021.02.008

545   Li, Z., Fei, M.-E., Huyan, C., Shi, X., 2021. Nano-engineered, Fly Ash-Based Geopolymer Composites: An
546   Overview. Resour. Conserv. Recy. 168, 105334. http://dx.doi.org/10.1016/j.resconrec.2020.105334

547   Liebscher, M., Lange, A., Schröfl, C., Fuge, R., Mechtcherine, V., Plank, J., Leonhardt, A., 2016. Impact of
548   the molecular architecture of polycarboxylate superplasticizers on the dispersion of multi-walled carbon
549   nanotubes in aqueous phase. J. Mat. Sci. 52(4), 2296-2307. http://dx.doi.org/10.1007/s10853-016-0522-
550   3

551   Lu, D., Zhong, J., 2022. Carbon-based nanomaterials engineered cement composites: a review. J. of
552   Infrastructure Preservation and Resilience 3(1). http://dx.doi.org/10.1186/s43065-021-00045-y

553   Lu, Z., Hou, D., Hanif, A., Hao, W., Li, Z., Sun, G., 2018. Comparative evaluation on the dispersion and
554   stability of graphene oxide in water and cement pore solution by incorporating silica fume. Cem. Concr.
555   Compos. 94, 33-42. http://dx.doi.org/10.1016/j.cemconcomp.2018.08.011

556   Metaxa, Z.S., Konsta-Gdoutos, M.S., Shah, S.P., 2013. Carbon nanofiber cementitious composites: Effect of
557   debulking procedure on dispersion and reinforcing efficiency. Cem. Concr. Compos. 36, 25-32.
558   http://dx.doi.org/10.1016/j.cemconcomp.2012.10.009

559   Motoyoshi, K., Yusuke, S., Takuya, S., 2022. Effect of pH and electrolyte concentration on sol–gel state of
560   semi-dilute aqueous cellulose nanofiber suspension: an interpretation based on angle-dependent DLVO
561   theory. Colloid. Polym. Sci. 300(8). http://dx.doi.org/10.1007/S00396-022-04999-7

562   Pan, Z., Sanjayan, J.G., Rangan, B.V., 2011. Fracture properties of geopolymer paste and concrete. Mag. Concr.
563   Res. 63(10), 763-771. http://dx.doi.org/10.1680/macr.2011.63.10.763

564   Qin, W., Guodong, Q., Dafu, Z., Yue, W., Haiyu, Z., 2021. Influence of the molecular structure of a
565   polycarboxylate superplasticiser on the dispersion of graphene oxide in cement pore solutions and
566   cement-based composites. Construct. Build. Mater. 272.
567   http://dx.doi.org/10.1016/j.conbuildmat.2020.121969

568   Rose, W.I., Durant, A.J., 2009. Fine ash content of explosive eruptions. J. Volcanol. Geotherm. Res. 186(1-2),
569   32-39. http://dx.doi.org/10.1016/j.jvolgeores.2009.01.010

570   Rovnaník, P., Šimonová, H., Topolář, L., Bayer, P., Schmid, P., Keršner, Z., 2016. Carbon nanotube reinforced

alkali-activated slag mortars. Construct. Build. Mater. 119, 223-229. http://dx.doi.org/10.1016/j.conbuildmat.2016.05.051

Sargam, Y., Wang, K., Tsyrenova, A., Liu, F., Jiang, S., 2021. Effects of anionic and nonionic surfactants on the dispersion and stability of nanoSiO2 in aqueous and cement pore solutions. Cem. Concr. Res. 144. http://dx.doi.org/10.1016/j.cemconres.2021.106417

Shi, T., Li, Z., Guo, J., Gong, H., Gu, C., 2019. Research progress on CNTs/CNFs-modified cement-based composites – A review. C Construct. Build. Mater. 202, 290-307. http://dx.doi.org/10.1016/j.conbuildmat.2019.01.024

Stephens, C., Brown, L., Sanchez, F., 2016. Quantification of the re-agglomeration of carbon nanofiber aqueous dispersion in cement pastes and effect on the early age flexural response. Carbon 107, 482-500. http://dx.doi.org/10.1016/j.carbon.2016.05.076

Wang, B.-M., Zhang, Y., Guo, Z.-Q., Han, Y., Ma, H.-N., 2012. Dispersion of Carbon Nanofibers in aqueous solution. Nano 7(6), 1250052-1-1250052-8. http://dx.doi.org/10.1142/S179329201250052X

Wang, B.-M., Zhang, Y., 2014. Synthesis and properties of carbon nanofibers filled cement-based composites combined with new surfactant methylcellulose. Mater. Express. 4(2), 177-182. http://dx.doi.org/10.1166/mex.2014.1157

Wang, Q., Qi, G.-d., Wang, Y., Zheng, H.-y., Shan, S.-h., Lu, C.-x., 2021. Research progress on the effect of graphene oxide on the properties of cement-based composites. New. Carbon. Mater. 36(4), 729-750. http://dx.doi.org/10.1016/s1872-5805(21)60071-9

Wang, Y., Xiao, R., Hu, W., Jiang, X., Zhang, X., Huang, B., 2021. Effect of granulated phosphorus slag on physical, mechanical and microstructural characteristics of Class F fly ash based geopolymer. Construct. Build. Mater. 291, 123287. http://dx.doi.org/https://doi.org/10.1016/j.conbuildmat.2021.123287

Wygel, C.M., Peters, S.C., McDermott, J.M., Sahagian, D.L., 2019. Bubbles and Dust: Experimental Results of Dissolution Rates of Metal Salts and Glasses From Volcanic Ash Deposits in Terms of Surface Area, Chemistry, and Human Health Impacts. Geohealth 3(11), 338-355. http://dx.doi.org/10.1029/2018GH000181

Xu, Z., Huang, Z., Liu, C., Deng, H., Deng, X., Hui, D., Zhang, X., Bai, Z., 2021. Research progress on key problems of nanomaterials-modified geopolymer concrete. Nanotechnol. Rev. 10(1), 779-792. http://dx.doi.org/10.1515/ntrev-2021-0056

Yazdanbakhsh, A., Grasley, Z., Tyson, B., Al-Rub, R.K.A., 2010. Distribution of Carbon Nanofibers and Nanotubes in Cementitious Composites. Trans. Res. Rec. 2142(1), 89-95. http://dx.doi.org/10.3141/2142-13

Yuan, J., He, P., Jia, D., Fu, S., Zhang, Y., Liu, X., Cai, D., Yang, Z., Duan, X., Wang, S., Zhou, Y., 2017. In situ processing of MWCNTs/leucite composites through geopolymer precursor. J. Eur. Ceram. Soc. 37(5), 2219-2226. http://dx.doi.org/10.1016/j.jeurceramsoc.2017.01.008

Zhang, R., Zhou, S., Li, F., Bi, Y., Zhu, X., 2022. Mechanical and Microstructural Characterization of Carbon Nanofiber–Reinforced Geopolymer Nanocomposite Based on Lunar Regolith Simulant. J. Mater. Civ. Eng. 34(1). http://dx.doi.org/10.1061/(asce)mt.1943-5533.0004025

Zhang, Y., Gong, H., Jiang, X., Lv, X., Xiao, R., Huang, B., 2021. Environmental impact assessment of pavement road bases with reuse and recycling strategies: A comparative study on geopolymer stabilized macadam and conventional alternatives. Transp. Res. D. Transp. Environ. 93, 102749. http://dx.doi.org/https://doi.org/10.1016/j.trd.2021.102749

Zhao, L., Guo, X., Liu, Y., Ge, C., Chen, Z., Guo, L., Shu, X., Liu, J., 2018. Investigation of dispersion behavior of GO modified by different water reducing agents in cement pore solution. Carbon 127, 255-269. http://dx.doi.org/10.1016/j.carbon.2017.11.016

Zhao, L., Zhu, S., Wu, H., Zhang, X., Tao, Q., Song, L., Song, Y., Guo, X., 2020. Deep research about the mechanisms of graphene oxide (GO) aggregation in alkaline cement pore solution. Construct. Build. Mater. 247. http://dx.doi.org/10.1016/j.conbuildmat.2020.118446

Zhou, S., Lu, C., Zhu, X., Li, F., 2021. Upcycling of natural volcanic resources for geopolymer: Comparative study on synthesis, reaction mechanism and rheological behavior. Construct. Build. Mater. 268. http://dx.doi.org/10.1016/j.conbuildmat.2020.121184